PHOTONICS Research

Optical topological lattices of Bloch-type skyrmion and meron topologies

QIANG ZHANG,[1] ![ORCID] ZHENWEI XIE,[1,2] ![ORCID] PENG SHI,[1] HUI YANG,[1] HAIRONG HE,[1] LUPING DU,[1,3] AND XIAOCONG YUAN[1,4]

[1]*Nanophotonics Research Center, Shenzhen Key Laboratory of Micro-Scale Optical Information Technology & Institute of Microscale Optoelectronics, Shenzhen University, Shenzhen 518060, China*
[2]*e-mail: ayst3_1415926@sina.com*
[3]*e-mail: lpdu@szu.edu.cn*
[4]*e-mail: xcyuan@szu.edu.cn*

Optical skyrmions, quasiparticles that are characterized by the topologically nontrivial vectorial textures of optical parameters such as the electromagnetic field, Stokes parameters, and spin angular momentum, have aroused great attention recently. New dimensions for optical information processing, transfer, and storage have become possible, and developing multiple schemes for manipulating the topological states of skyrmions, thus, is urgent. Here we propose an approach toward achieving dynamic modulation of skyrmions via changing the field symmetry and adding chirality. We demonstrate that field symmetry governs the skyrmionic transformation between skyrmions and merons, whereas material chirality modulates the twist degree of fields and spins and takes control of the Néel-type–Bloch-type skyrmionic transition. Remarkably, the enantioselective twist of skyrmions and merons results from the longitudinal spin arising from the chirality-induced splitting of the hyperboloid in the momentum space. Our investigation, therefore, acts to enrich the portfolio of optical quasiparticles. The chiral route to topological state transitions will deepen our understanding of light–matter interaction and pave the way for chiral sensing, optical tweezers, and topological phase transitions in quantum matter. © 2022 Chinese Laser Press

https://doi.org/10.1364/PRJ.447311

1. INTRODUCTION

The topology of electromagnetic waves is at the focus of booming research efforts currently [1,2], in particular with respect to the possibility of emulating and exploiting topological phenomena typically emerged in particle physics and condensed matter, for example, skyrmions [Fig. 1(a)]. The concept of skyrmions was proposed by British physicist Tony Skyrme in the 1960s to account for the topological stability of particles that are characterized by a topological integer number that cannot be changed by a continuous deformation of the field configuration [4]. Now it has been introduced to the realm of optics. The very recent discoveries of optical skyrmions in surface plasmon polaritons (SPPs) [5,6], therefore, opened a new chapter in nanophotonics and endowed a new perspective to control structured light and light–matter interactions [7,8].

The fascinating vectorial textures of electric field [5] and spin angular momentum (SAM) [6] immediately triggered people's interest in unveiling their ultrafast dynamic behavior [9,10]. Subsequent efforts of mapping and manipulating the plasmonic skyrmions were reported as well [11–15]. Moreover, optical skyrmions have also been constructed by Dirac monopoles in momentum space [16], Stokes vectors

in free space [17–20] and microcavities [21], pseudospins in 3D nonlinear photonic crystals [22], and Raman transitions [23] and electric or magnetic field vectors in spatiotemporal optical pulses [24]. Later, a similar kind of quasiparticles called merons [Fig. 1(a)], also known as half-skyrmions, was reported as can be found in the momentum space in photonic crystals [25], liquid crystal filled microcavities [26], SPPs in an Archimedean coupling structure [10] and symmetry governed evanescent optical vortex lattices [27]. Meanwhile, a single free-space bimeron is for the first time obtained via Stokes vector fields in well-designed structured vector beams [28]. Note that skyrmions and bimerons are theoretically isomorphic with the same integer skyrmion number (±1), but merons are topologically different with them due to the half-skyrmion number ($\pm1/2$) [28].

Whereas a number of works have studied Néel-type skyrmions in electromagnetic waves, not much is known about the topological properties of the Bloch-type skyrmions, or the Bloch-type merons in particular. Here we show that the Bloch-type skyrmion configuration can be created simply by adding chirality. Consider the more general case where an evanescent optical vortex (e-OV) with the topological charge $l = 1$ results
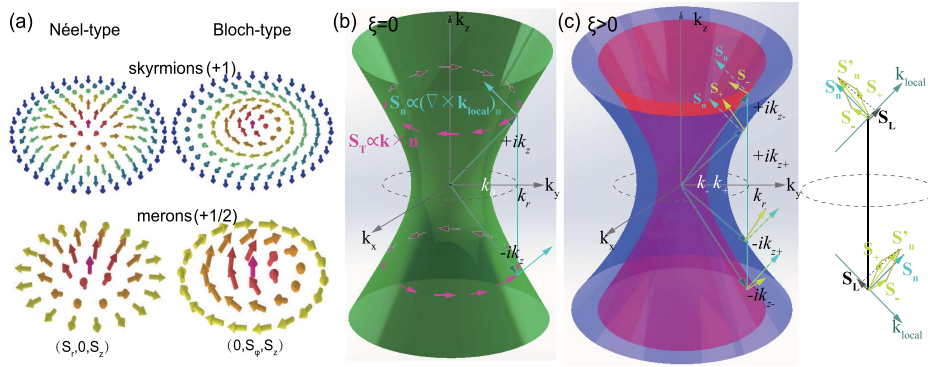
Fig. 1.   Skyrmions/merons and the origin of longitudinal spin due to chirality. (a) Artistic illustrations of Néel- and Bloch-type skyrmions and merons (figure fashions followed Ref. [3]). (b) For the evanescent wave in a nonchiral system with $k_x^2 + k_y^2 = k_r^2 > k^2$, the transverse spin $\mathbf{S_T} \propto \mathbf{k} \times \mathbf{n}$, the normal spin component $\mathbf{S_n} \propto (\nabla \times \mathbf{k_{local}})_n$, and the wave vector satisfies $k_x^2 + k_y^2 + (ik_z)^2 = k^2$, corresponding to a hyperboloid in the k-space. In the case that $\pm k_z$ correspond to evanescent waves in the upper and lower sides of interface, the transverse spin is locked with the momentum (spin-momentum locking) and reverses its sign across the boundary. However, in a (c) chiral system, as circularly polarized light is always an eigenmode of an isotropic medium, the introduction of chirality splits the hyperboloid into two (one resides inside and the other outside the nonchiral hyperboloid): $k_x^2 + k_y^2 - k_{z\pm}^2 = k_\pm^2$, corresponding to LCP and RCP waves, respectively. The normal spin component $\mathbf{S_n'}$, thus, also is separated into $\mathbf{S_-}$ and $\mathbf{S_+}$ due to the symmetry breaking [in this case $\mathbf{S_n'} = \mathbf{S_-} + \mathbf{S_+}$ and spin vectors $\vec{a}_1 \cdot \vec{b}_1 = 0$, $\vec{a}_2 \cdot \vec{b}_2 = 0$ but $(\vec{a}_1 + \vec{a}_2) \cdot (\vec{b}_1 + \vec{b}_2) \neq 0$]. This yields an extra spin component, which is perpendicular to $\mathbf{S_n}$, i.e., the longitudinal spin $\mathbf{S_L}$, which is parallel to the momentum ($\mathbf{k_{local}}$). Most importantly, this longitudinal spin does not obey the spin-momentum locking rule and will not change sign across the boundary. Its sign solely depends on the sign of material's chirality.

in an isolated spin skyrmion [6] (dynamic field skyrmions can be regarded as created in an $l = 0$ plasmonic system in the absence of spin–orbit coupling but in a lattice form [5]): in a nonchiral system with $k_x^2 + k_y^2 = k_r^2 > k^2$ (evanescent wave), the wave vector satisfies $k_x^2 + k_y^2 - k_z^2 = k^2$, corresponding to a hyperboloid in the k-space [Fig. 1(b)]. The spin textures can be decomposed into a transverse part and a normal part, which are determined by $\mathbf{S_T} \propto \mathbf{k} \times \mathbf{n}$ [29–31] and $\mathbf{S_n} \propto (\nabla \times \mathbf{k_{local}})_n$ ($\mathbf{k_{local}}$ the local wave vector) [6,32], respectively [Figs. 1(a) and 1(b)]. On the upper and lower sides of a metal-dielectric interface or near the upper ($-ik_z$) and lower ($+ik_z$) sides of a dielectric sandwiched between two metals [metal-dielectric-metal (MDM)], the transverse spin is locked with the energy flow (spin-momentum locking) and reverses its sign across the boundary [30,31]. And since the transverse spin is always orthogonal to the energy flow ($\mathbf{P_o} = \mathbf{k_{local}}\hbar$), for e-OVs it corresponds to the radial spin S_r in the cylindrical coordinate system [Fig. 1(a)]. The skyrmions are always Néel type.

However, as circularly polarized light is always an eigenmode of an isotropic chiral medium, the introduction of chirality splits the hyperboloid into two: $k_x^2 + k_y^2 - k_{z\pm}^2 = k_\pm^2$, with $k_\pm = (n_0 \pm \xi)k_0$ (ξ the chirality parameter). For a well-confined k_r, the normal spin component $\mathbf{S_n}$, thus, is separated into $\mathbf{S_-}$ and $\mathbf{S_+}$ due to the chirality-dependent excess of either the LCP component or RCP component. As a result, $\mathbf{S_-} + \mathbf{S_+}$ is not normal to the synthetic wave vector anymore in the chiral medium, and an extra spin component that is perpendicular to $\mathbf{S_n}$ and parallel to the wave vector is generated, i.e., the longitudinal spin $\mathbf{S_L}$ [Fig. 1(c)]. Most importantly, this longitudinal spin does not obey the spin-momentum locking rule and will not change sign as long as in the chiral medium. The sign solely depends on the handedness of material's chirality. For e-OVs in the chiral medium, such non-vanishing longitudinal spin (along the energy flow; for an evanescent/plasmonic optical

vortex, $\mathbf{P_o}$ is azimuthally revolving around the vortex singularity) corresponds to S_φ in the cylindrical coordinate system [Fig. 1(a)] and provides the possibility of the emergence of Bloch-type skyrmion configuration. Our work is, thus, driven by this major principle.

On the other hand, the twist evolutions of the local vectors in skyrmions are chiral geometrically [33–35], and so are they in the optical field and spin skyrmions in SPPs. Typically, enantioselective responses take place in the interaction between chiral entities (e.g., skyrmions) and chiral materials with opposite chirality. Our interest of investigating the skyrmion-chiral material interaction is also driven by this secondary principle.

To this end, we combine the twist degree of freedom in both material and optical skyrmions. The paper is organized as follows. We first show in a tri-layered hexagonal plasmonic coupling structure [metal-chiral-metal (MCM)] the degenerated case ($l = 0$), the field skyrmion lattices. We show that the Bloch-type field skyrmion lattice is possible in the structure center due to the field mode symmetry and chirality-induced field mode hybridization. We note that such skyrmions and merons in the real space and spin space of SPPs have never been reported. We then show in a square plasmonic coupling structure that Bloch field meron lattices also exist. Finally, we demonstrate that similar scenario occurs for the spin skyrmion and meron lattices ($l = 1$). The two scenarios share the same underlying physics: symmetry governed skyrmion to meron transformation and chirality-induced twist of fields and spins in skyrmions and merons. We proved our theory for longitudinal spin induced Bloch-type skyrmion topology via rigorous derivations based on Maxwell's equations.

In addition to fundamental insights, our studies enlarge the portfolio of optical skyrmions which so far have demonstrated promises in deep-subwavelength metrology [6,36], topological Hall devices [22], precise control over resonant modes in nano-

structures [37], high harmonic generations [38], optical tweezers [11], cold atom lattice-alike skyrmion trapping [39], and magnetic domain detection [40].

2. BLOCH-TYPE ELECTRIC FIELD SKYRMION LATTICES

It is known that, for the three layer case where the sandwiched medium is nonchiral and for the single interface case where the medium filling the lower half space is nonchiral, optical skyrmions in electromagnetic fields of SPPs are purely Néel-type [41,42]. Introducing chirality to such a single interface plasmonic system leads to hybrid TM-TE mode SPPs. But the field skyrmions are still Néel-type, or more precisely the so-called twisted-Néel-type. However, we propose that inside a multilayered structure such as the MCM waveguide, there exists a special Néel–Bloch–Néel-type evolution.

We first consider a one-dimensional (1D) MCM structure where the SPPs propagate along the x axis and exponentially decay along the z axis [see Fig. 2(a)]. Spin topologies in this case are degenerated in dynamic field skyrmions due to the absence of spin–orbit coupling. For the symmetric mode, the distribution of E_z across the boundaries ($z = \pm d$ and $d = 5$ nm) is symmetric, while E_x is antisymmetric and vanishes in the center ($z = 0$). The mode hybridization due to chirality results in the emergence of E_y component, and it has a symmetric distribution. More interestingly, for SPPs at a single chiral-metal interface, E_y reverses its sign for opposite handedness of chirality [43], which occurs in the same manner for the MCM case as can be inspected by simply considering just one of the six SPP waves in Eq. (1). As a consequence, at $z = 0$, the electric field vectors take the form $(0, \pm E_y, E_z)$ for $\pm \xi$. Extending such 1D case to two-dimensional (2D), therefore, will result in the in-plane electric field components that are perpendicular to the radial directions at $z = 0$ [Fig. 2(b)]. In consequence, for a hexagonal lattice, the electric field skyrmions are Bloch-type.

We further prove this by rigorous deductions. The plasmonic coupling structure in Fig. 2(a) has been widely applied both in the excitation and observation of optical skyrmions [5,9,11] and acoustic skyrmions [44]. The light source ($\lambda_0 = 633$ nm) can be six coherent laser beams with tunable phase relationships. One feasible way to produce such a light source is using one spatial light modulator to define the phases of the six beams and then using a wavelength plate consisting of six half-wavelength plates to adjust the incident polarization direction of the light field [45,46]. Drude model for the permittivity of gold is adopted [47]. The isotropic chiral material is modeled using the following constitutive relation [48]: $\mathbf{D} = \epsilon_c \mathbf{E} + i\xi\sqrt{\mu_0\epsilon_0}\mathbf{H}$, $\mathbf{B} = \mu_0\mathbf{H} - i\xi\sqrt{\mu_0\epsilon_0}\mathbf{E}$, where ϵ_c is the permittivity of the chiral material. $\xi = \pm 0.15$ are adopted to the same order of magnitude as in Ref. [49] for demonstration (the available chiral materials can be a polycrystalline film of chlorophyll a, as demonstrated in Ref. [49]) in this paper. $k_\pm = (\sqrt{\epsilon_c/\epsilon_0} \pm \xi)\omega/c$ are eigen-wavenumbers corresponding to the right-handed circularly polarized (RCP) and left-handed circularly polarized (LCP) waves, respectively. Using Bohren decompositions [50], $\mathbf{F}_\pm = \mathbf{E} \pm i\eta\mathbf{H}$ ($\eta = \sqrt{\mu_0/\epsilon_c}$ is the wave impedance of the chiral medium), and the field equations then satisfy $\nabla \cdot \mathbf{F}_\pm = 0$, $\nabla \times \mathbf{F}_\pm = \pm k_\pm \mathbf{F}_\pm$, and $\nabla^2 \mathbf{F}_\pm + k_\pm^2 \mathbf{F}_\pm = 0$, with $\mathbf{E} = (\mathbf{F}_+ + \mathbf{F}_-)/2$ and $\mathbf{H} = (\mathbf{F}_+ - \mathbf{F}_-)/2i\eta$. Therefore, the electric field interference pattern in the chiral material can be derived as (where the time convention $e^{-i\omega t}$ is omitted)

$$
\begin{aligned}
E_z = \sum_{i=1}^{3} \Big[& F_{+1} e^{-k_{z+}(z+d)} + F_{-1} e^{-k_{z-}(z+d)} \\
& + F_{+2} e^{k_{z+}(z-d)} + F_{-2} e^{k_{z-}(z-d)} \Big] \\
& \times e^{i\frac{\varphi_i + \varphi_{i+3}}{2}} \cos\left(k_{xi}x + k_{yi}y + \frac{\varphi_i - \varphi_{i+3}}{2} \right),
\end{aligned} \quad \textbf{(1)}
$$

where $F_{\pm 1,2}$ denote the amplitude at the top and bottom interfaces (for a symmetric MCM structure, $F_{+1} = F_{+2}$,
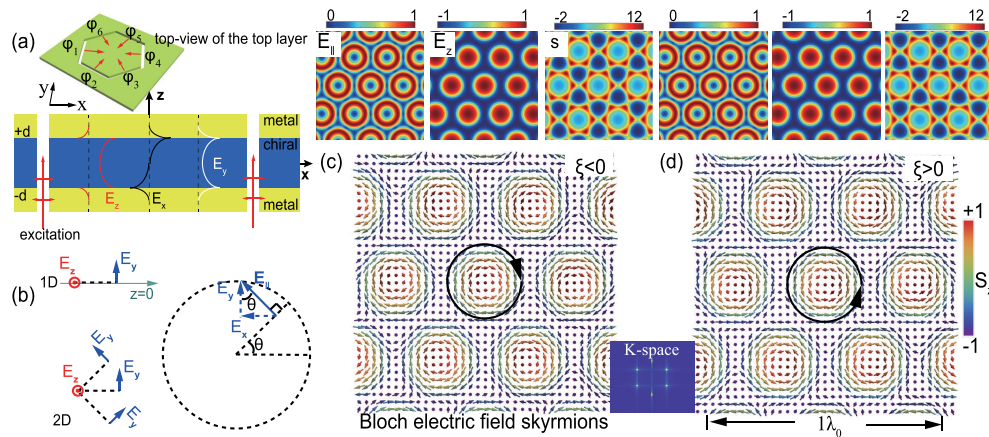

Fig. 2. Calculated Bloch-type electric field skyrmion lattices. (a) Top-viewed hexagonal plasmonic coupling pattern and side-viewed typical electric field distributions in an MCM structure. (b) Field vectorial orientations for 1D and 2D chiral SPPs (at $z = 0$), respectively. For a Bloch-type skyrmion, the in-plane field vectors are oriented as such. (c), (d) Bloch electric field skyrmion lattices (when $\varphi_{1,2,\ldots,6} = 0$) for $\xi < 0$ and $\xi > 0$, respectively. Top panel insets, shown from left to right, are the in-plane component, out-of-plane component, and the skyrmion number density (μm^{-2}) distribution of the electric field.

$F_{-1} = F_{-2}$), k_r the parallel-component of the wave vector, $ik_{z\pm}$ the out-of-plane component of the wave vector, maintaining the relation $k_r^2 + (ik_{z\pm})^2 = k_\pm^2$, and φ_i the phase of SPPs from each slit. $k_{xi} = k_r \cos\theta_i$, $k_{yi} = k_r \sin\theta_i$ with $\theta_1 = \pi/6$, $\theta_2 = \pi/2$, and $\theta_3 = 5\pi/6$. The SPP wavenumber k_r is then evaluated as the eigenvalue solution of the dispersion relation. More details on the derivation are given in Appendix A. Note that in general the electric field is complex valued in lossy systems. However, for small losses, the imaginary part is negligible and does not affect the real part, and the skyrmion topology is robust against losses [5,6]. The field equations in Eq. (1) are more general than the nonchiral field expression in Ref. [5] as they can reduce into nonchiral ones when $\xi = 0$ and phase modulation of each excitation slit is also considered.

Hence, according to Eq. (1) and Appendix A, at any location in the x–y plane at $z = 0$, $E_{yi}/E_{xi} = -k_{xi}/k_{yi} = -\cot\theta_i$ ($i = 1, 2, 3$). Field vectors obeying this relation orient orthogonally to the radial direction, as illustrated in the rightmost graph of Fig. 2(b). We then visualize the electric field vectors based on Eq. (1) in Figs. 2(c) and 2(d), where clear characteristics of the Bloch-type skyrmions can be seen. When the dielectric is chiral, mode hybridization for SPPs emerges, resulting in differential $k_\pm$, $k_{z\pm}$, and $F_\pm$. Substantial inequality between the RCP and LCP portion of the SPPs contributes to the opposite twist of skyrmions for $\pm\xi$. The chiral twist (clockwise for $\xi < 0$ and counterclockwise for $\xi > 0$) can be more easily understood in 1D SPPs at a chiral-metal interface as pointed out in Ref. [43], where opposite E_y components emerge for ξ with opposite signs for 1D SPPs propagating along x direction and decaying toward z direction. That can be considered as opposite twist along $\pm y$ compared with 1D nonchiral SPPs.

To further verify the skyrmion analogy, we calculate the skyrmion number density (s) of the electric vector structure $s = \frac{1}{4\pi}\mathbf{e} \cdot (\frac{\partial \mathbf{e}}{\partial x} \times \frac{\partial \mathbf{e}}{\partial y})$, where $\mathbf{e} = (\cos\phi(\theta)\sin\alpha(r), \sin\phi(\theta)\sin\alpha(r),$

$\cos\alpha(r))$ represents the unit vector in the direction of the local electric field in the plane $z = 0$. The skyrmion number density distribution is plotted in the top panel of Figs. 2(c) and 2(d). Integrating over every lattice site enables us to evaluate the skyrmion number of the lattice, which is 1 for each individual skyrmion. Additionally, one can also characterize the swirling structure of a skyrmion via its topology by calculating the skyrmion number (N) as $N = \frac{1}{4\pi}\iint \mathbf{e} \cdot (\frac{\partial \mathbf{e}}{\partial x} \times \frac{\partial \mathbf{e}}{\partial y})dxdy$, which can eventually be expressed as $N = -\frac{1}{4\pi}\cos\alpha(r)|_{\alpha(0)}^{\alpha(r_1)} \times \phi(\theta)|_{\theta=0}^{\theta=2\pi}$ [51], $\phi(\theta)|_{\theta=0}^{\theta=2\pi} \equiv 2\pi$. For a photonic spin structure with the electric vector changing progressively from the "up" state [$\cos\alpha(0) = 1$] to the "down" state [$\cos\alpha(r_1) = -1$] at each lattice site, the skyrmion number can be evaluated as $N = 1$, regardless of the value of ξ. Therefore, numerical integration of the skyrmion number density and analytical quantification of the skyrmion number according to the electric vector topology simultaneously confirm the skyrmion feature of the electric field, no matter how it is twisted.

3. SKYRMIONIC TRANSFORMATION BETWEEN FIELD SKYRMION AND MERON LATTICES

Altering the phase relationships among each excitation slit provides extra degree of freedom in tailoring the optical skyrmion lattice. This stems directly from the variation of interference patterns between the three pairs of SPP standing waves. For example, increasing one of the three pairs of the slits' phase by π (e.g., $\varphi_2 = \varphi_5 = \pi$) results in the lateral translation of skyrmion lattice by a unit cell along that direction [13,44]. Note that in this case the skyrmion number of each cell becomes –1 immediately due to the core-up (central spin vector pointing straight up) to core-down transition (central spin vector pointing straight down).

Here, it is worthwhile to mention that by setting $\varphi_2 = \pi$, meron lattice, that is half-skyrmion lattice, emerges inside a
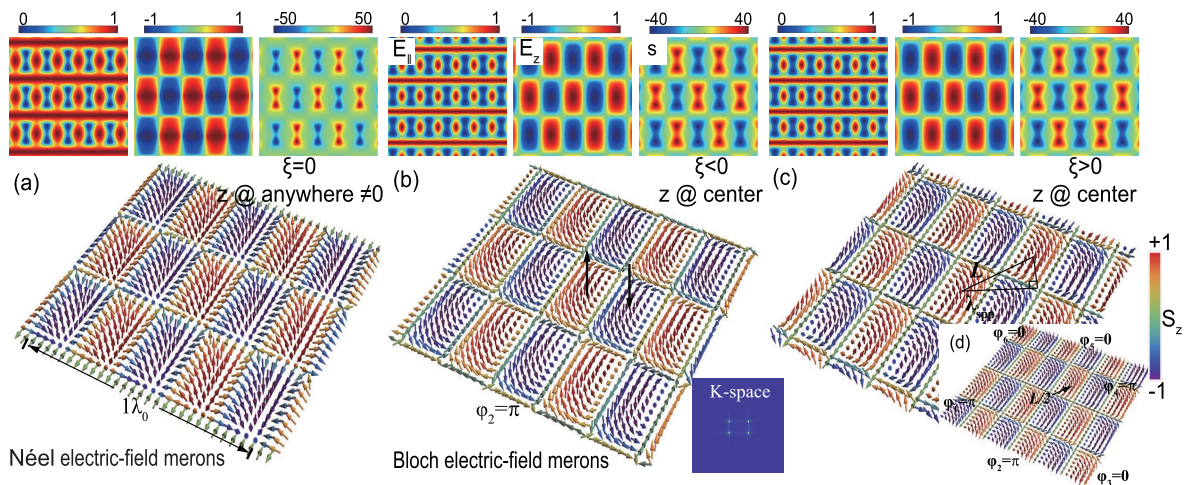

Fig. 3. Tailoring the skyrmion lattice by phase modulation and the formation of Bloch electric field meron lattice. A novel optical meron lattice, i.e., half-skyrmion lattice with each unit cell's skyrmion number equal to either –1/2 or +1/2, can be generated by tuning the phase of excitation, such as setting $\varphi_2 = \pi$ and the phases of the rest of the boundaries 0. (a) For an MIM structure, Néel-type electric field meron lattices can be found inside the insulator at anywhere except the center. (b), (c) Bloch electric field meron lattices for $\xi < 0$ and $\xi > 0$, respectively. Chirality dependent twist of meron textures can also be observed here. (d) Manipulation of meron lattices by tuning the phases of the SPPs at the boundaries.

well-defined rectangular perimeter [see Fig. 3(a)]. Besides, in this case, merons exist in pairs with alternating skyrmion numbers of $-1/2$ and $+1/2$ distributed over the lattice, namely, meron pairs. The inset on the left-hand side above Fig. 3(a) illustrates the in-plane electric field distribution for a meron lattice in a conventional MDM structure, which is purely Néel-type, resembling of the dumb-bell like spin texture that was recently found in the isolated plasmonic spin meron [10]. In this case, $\cos \alpha(0) = +1$ (or -1) as the merons are core-up (or core-down) and $\cos \alpha(r_1) = 0$ as the electric vectors are in-plane along the perimeter, so $N = -\frac{1}{4\pi} \cos \alpha(r)|_{\alpha(0)}^{\alpha(r_1)} \times \phi(\theta)|_{\theta=0}^{\theta=2\pi} = \pm 1/2$. Note that the merons shown here with skyrmion number $N = -1/2$ are not antimerons; they are topologically equivalent to merons with $N = +1/2$.

A similar scenario arises after introducing chirality to the system. As shown in Figs. 3(b) and 3(c), opposite twist degree of freedom can be exerted by opposite handedness of chirality to the Bloch-type field merons. Here we take the phase modulation of $\varphi_2 = \pi$ as an example. In effect, due to the various orientation angles of each pair of the SPP standing waves ($\theta = \pi/6$, $\pi/2$, and $5\pi/6$), one can obtain the dynamic control of skyrmion lattice in three different directions. Moreover, phase tailoring of more than one of the three slit pairs enables multiple extra control combinations. For example, if we set the phases of the SPPs at the boundaries as $\varphi_2 = \pi$ and $\varphi_1 = \varphi_4 = \pi$, the skyrmion configuration becomes a meron lattice that is shifted along the direction between boundaries 1 and 4 by $L/2 = \lambda_{spp}/\sqrt{3}$, as given in Fig. 3(c) and its inset, Fig. 3(d). Therefore, such a type of plasmonic structure would offer us excessive degrees of freedom to manipulate optical skyrmions and merons, and thereby facilitate their future applications such as in quantum information transducing and data storage.

4. BLOCH SPIN SKYRMION AND MERON LATTICES

Spin skyrmions in vortex SPPs originate from the transverse spin and the total angular momentum conservation

[6,32,52]. The spin textures of a single plasmonic vortex at a chiral-metal surface constitute an isolated twisted-Néel-type skyrmion. By suitably designing a thin chiral optical waveguide, a single Bloch spin skyrmion can appear as the preserved waveguide eigenmode [53]. This is closely related to the chirality dependent "longitudinal" spin in contrast to the conventional transverse spin [30,31], while a plasmonic vortex lattice can exhibit distinct spin topologies due to the symmetry of the field [27,52]. Here we go further by demonstrating the chirality-dependent Bloch spin skyrmion/meron lattices, which have yet to be found in the novel domain of optical skyrmions.

Individual optical spin-skyrmions formed due to the spin–orbit coupling in the chiral-metal evanescent field can be described by Hertz-like vector potentials with a helical phase term in the cylindrical coordinate (r, φ, z) as $f_{z\pm} = a_{\pm} J_l(k_r r) \cdot e^{il\varphi} e^{-k_{z\pm} z}$ [53], where $a_{\pm}$ is a constant, k_r and $ik_{z\pm}$ are the transverse and longitudinal wave vector components satisfying $k_r^2 - k_z^2 = k_{\pm}^2$ with $k_{\pm} = (n \pm \xi)k_0$ being the eigen wave vectors in chiral medium, and J_l is the Bessel function of the first kind of order l.

We first focus on the hexagonal optical vortex lattice. Taking the rotational and translational symmetry of an $l = 1$ hexagonal vortex lattice into account, the superposition of each individual Hertz-like vector potential with each lattice point leads to the spin skyrmion lattice. After deduction of the electromagnetic field equations, we obtain the corresponding SAM expression as (more details on the derivation are given in Appendices B and C):

$$S_z = \frac{\varepsilon}{8\omega}\{[a_{1+}e^{-k_{z+}(z+d)} + a_{2+}e^{k_{z+}(z-d)}]^2 + [a_{1-}k_- e^{-k_{z-}(z+d)} + a_{2-}e^{k_{z-}(z-d)}]^2\}S_{z0}, \quad (2)$$

where S_{z0} represents the nonchiral-metal SAM terms. Interestingly, S_{z0} consists of two subsets of optical vortices with different wave vector values ($K = k_r$ and $K = \sqrt{3}k_r$) in the momentum space [27], respectively:
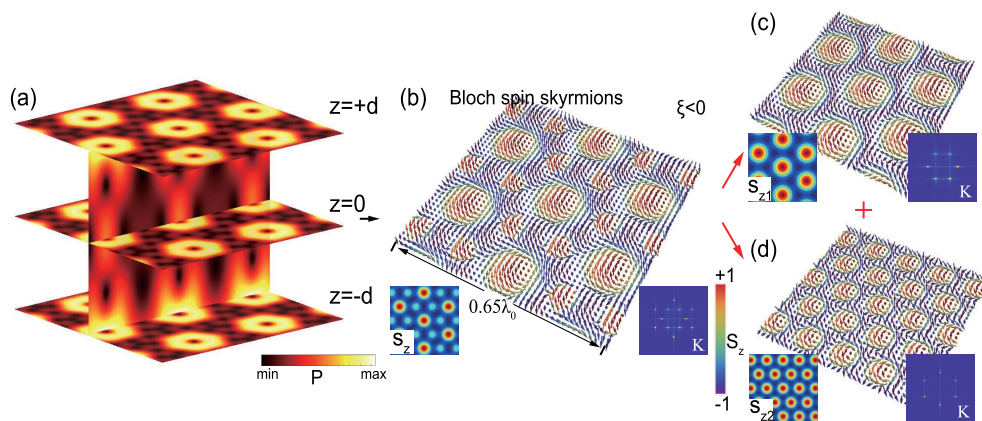

Fig. 4. Optical Bloch-type spin skyrmion lattice. (a) Unique energy flow distribution is an MCM structure for a hexagonal plasmonic vortex lattice. (b) Calculated vectorial representation of a Bloch spin skyrmion lattice containing (c), (d) two subsets of Bloch spin skyrmion lattices. Each sub-spin skyrmion lattice consists of skyrmions with same skyrmion number $N = 1$. The insets describe the out-of-plane component of the SAM S_z in the real space and momentum space.
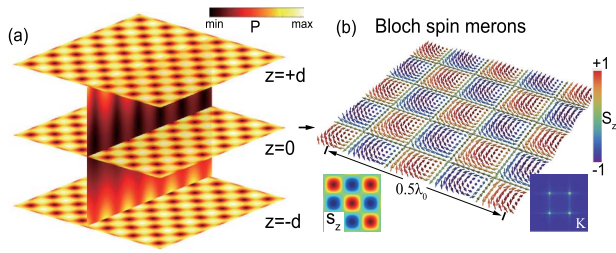
Fig. 5. Optical Bloch-type meron lattice. (a) Energy flow distribution is an MCM structure for a square plasmonic vortex lattice. (b) Optical spin orientation distribution showing a meron lattice.

$$S_{z0} = \cos(k_r x) + \cos(\sqrt{3} k_r y)$$
$$+ \cos\left(\frac{1}{2} k_r x + \frac{\sqrt{3}}{2} k_r y\right) + \cos\left(\frac{1}{2} k_r x - \frac{\sqrt{3}}{2} k_r y\right)$$
$$+ \cos\left(\frac{3}{2} k_r x + \frac{\sqrt{3}}{2} k_r y\right) + \cos\left(\frac{3}{2} k_r x - \frac{\sqrt{3}}{2} k_r y\right). \quad (3)$$

The energy flow [$\mathbf{P} = \mathrm{Re}(\mathbf{E}^* \times \mathbf{H})/2$] of the vortices can, therefore, be visualized as given in Fig. 4(a). Such unique energy flow distribution determines the topology of spin textures, as shown in Fig. 4(b), which exhibit exactly the Bloch-type skyrmionic feature at $z = 0$. Similarly, the Bloch spin skyrmion lattice can also be decomposed into two subsets of optical vortex lattices with skyrmionic spin textures shown in Figs. 4(c) and 4(d). We also show the k-space distribution of the wave vectors in the insets. Each subset contains a spin skyrmion lattice with each individual skyrmion (also Bloch type) having the same skyrmion number $N = 1$ and the same in-plane twist induced by the material chirality.

On the other hand, when such a hexagonal lattice is transformed to a square lattice, the formation of an optical spin meron lattice takes place. For such a square plasmonic vortex lattice in the MCM structure, we also derived the explicit electromagnetic field equations and finally obtained the SAM expression as (more details on the derivation are given in Appendix D):

$$S_z = \frac{\varepsilon}{8\omega}[\cos(k_r x + k_r y) + \cos(k_r x - k_r y)]$$
$$\times \{[a_{1+}e^{-k_{z+}(z+d)} + a_{2+}e^{k_{z+}(z-d)}]^2$$
$$+ [a_{1-}e^{-k_{z-}(z+d)} + a_{2-}e^{k_{z-}(z-d)}]^2\}. \quad (4)$$

We present the energy flow in square symmetry in Fig. 5(a), and the meron spin lattice with alternating "core-up" and "core-down" spin meron topologies in Fig. 5(b). Along the peripheries of each unit square spin meron, the spin vectors are all parallel to the perimeters. Notably, this marks the Bloch-type analogy.

5. CONCLUSION

To conclude, we have introduced a new twist degree of freedom to both the optical field and spin skyrmion lattices using material's chirality. Changing the field symmetry from sixfold

(hexagonal) to fourfold (square) can transform the skyrmion lattice to meron (half-skyrmion) lattices for the topological textures of both the electric field vectors and the SAM vectors. In particular, to the best of our knowledge, the first optical analog of the Bloch-type skyrmion and meron field and spin lattices have been presented in this article. We note that our results and conclusions can also be exploited in THz regime [14,54] and materials with anisotropy such as hyperbolic metamaterials [55] and twisted bilayer 2D materials [56,57] or with magneto-optical effect [40], and in these materials many more fascinating topological effects would take place [58–62]. Therefore, our investigation has the potential to unlock new perspectives for studies of light–matter interactions in quantum chiral materials. The new topological features of electromagnetic waves may also open the door to the use of topological light for both classical and quantum information processing and sensing.

APPENDIX A: FIELD SKYRMION LATTICE IN A METAL-CHIRAL-METAL STRUCTURE

Chiral medium is located at $-d \leq z \leq +d$. For positively propagating SPPs,

$$F_{+x1} = \frac{1}{k_r^2}(-k_x k_{z+} + ik_y k_+)F_{+1}e^{ik_{z+}(z+d)}e^{i\varphi_1}e^{ik_x x + ik_y y}$$
$$+ \frac{1}{k_r^2}(k_x k_{z+} + ik_y k_+)F_{+2}e^{-ik_{z+}(z-d)}e^{i\varphi_1}e^{ik_x x + ik_y y},$$
$$F_{+y1} = \frac{-1}{k_r^2}(ik_x k_+ + k_y k_{z+})F_{+1}e^{ik_{z+}(z+d)}e^{i\varphi_1}e^{ik_x x + ik_y y}$$
$$+ \frac{-1}{k_r^2}(ik_x k_+ - k_y k_{z+})F_{+2}e^{-ik_{z+}(z-d)}e^{i\varphi_1}e^{ik_x x + ik_y y},$$
$$F_{+z1} = F_{+1}e^{ik_{z+}(z+d)}e^{i\varphi_1}e^{ik_x x + ik_y y}$$
$$+ F_{+2}e^{-ik_{z+}(z-d)}e^{i\varphi_1}e^{ik_x x + ik_y y}. \quad (A1)$$

For negatively propagating SPPs,

$$F_{-x1} = \frac{-1}{k_r^2}(k_x k_{z-} + ik_y k_-)F_{-1}e^{ik_{z-}(z+d)}e^{i\varphi_1}e^{ik_x x + ik_y y}$$
$$+ \frac{-1}{k_r^2}(-k_x k_{z-} + ik_y k_-)F_{-2}e^{-ik_{z-}(z-d)}e^{i\varphi_1}e^{ik_x x + ik_y y},$$
$$F_{-y1} = \frac{-1}{k_r^2}(-ik_x k_+ + k_y k_{z-})F_{-1}e^{ik_{z-}(z+d)}e^{i\varphi_1}e^{ik_x x + ik_y y}$$
$$+ \frac{-1}{k_r^2}(-ik_x k_- - k_y k_{z-})F_{-2}e^{-ik_{z-}(z-d)}e^{i\varphi_1}e^{ik_x x + ik_y y},$$
$$F_{-z1} = F_{-1}e^{ik_{z-}(z+d)}e^{i\varphi_1}e^{ik_x x + ik_y y}$$
$$+ F_{-2}e^{-ik_{z-}(z-d)}e^{i\varphi_1}e^{ik_x x + ik_y y}. \quad (A2)$$

Therefore, the electric field (with $k_{z\pm}$ replaced by $ik_{z\pm}$) can be written as

$$E_x = \frac{1}{k_r^2} \sum_{i=1}^{3} [F_{+1}(k_{xi}k_{z+} - k_{yi}k_+)e^{-k_{z+}(z+d)}$$

$$+ F_{-1}(k_{xi}k_{z-} + k_{yi}k_-)e^{-k_{z-}(z+d)}$$

$$+ F_{+2}(-k_{xi}k_{z+} - k_{yi}k_+)e^{k_{z+}(z-d)}$$

$$+ F_{-2}(-k_{xi}k_{z-} + k_{yi}k_-)e^{k_{z-}(z-d)}]$$

$$\times e^{i\frac{\varphi_i+\varphi_{i+3}}{2}} \sin\left(k_{xi}x + k_{yi}y + \frac{\varphi_i - \varphi_{i+3}}{2}\right),$$

$$E_y = \frac{1}{k_r^2} \sum_{i=1}^{3} [F_{+1}(k_+k_{xi} + k_{yi}k_{z+})e^{-k_{z+}(z+d)}$$

$$+ F_{-1}(-k_-k_{xi} + k_{yi}k_{z-})e^{-k_{z-}(z+d)}$$

$$+ F_{+2}(k_+k_{xi} - k_{yi}k_{z+})e^{k_{z+}(z-d)}$$

$$+ F_{-2}(-k_-k_{xi} - k_{yi}k_{z-})e^{k_{z-}(z-d)}]$$

$$\times e^{i\frac{\varphi_i+\varphi_{i+3}}{2}} \sin\left(k_{xi}x + k_{yi}y + \frac{\varphi_i - \varphi_{i+3}}{2}\right). \tag{A3}$$

At $z = 0$, and for a symmetric MCM structure $F_{+1} = F_{+2} = F_+$, $F_{-1} = F_{-2} = F_-$. $k_{xi} = k_r \cos \theta_i$ and $k_{yi} = k_r \sin \theta_i$. We then have

$$E_x = \frac{1}{k_r^2} \sum_{i=1}^{3} [-2F_+(k_r \sin\theta_i k_+) + 2F_-(k_r \sin\theta_i k_-)]$$

$$\times \sin(k_r \cos\theta_i x + k_r r \sin\theta_i y),$$

$$E_y = \frac{1}{k_r^2} \sum_{i=1}^{3} [2F_+(k_+k_r \cos\theta_i) + 2F_-(-k_-k_r \cos\theta_i)]$$

$$\times \sin(k_r \cos\theta_i x + k_r \sin\theta_i y). \tag{A4}$$

Therefore, $E_{yi}/E_{xi} = -k_{xi}/k_{yi} = -\cot\theta_i$ ($i = 1, 2, 3$).

APPENDIX B: MONOCHROMATIC BESSEL BEAMS IN CHIRAL MEDIUM AND SYMMETRY CONSIDERATIONS

In this section, we show in two ways that, in chiral medium, the RCP and LCP eigenmodes of a Bessel vortex beam possess the same rotational and translational symmetry simultaneously.

First, we start from Maxwell's equations: $\mathbf{F}_\pm$ field of a vortex beam in the chiral medium has mode solution as

$$\mathbf{F}_\pm = \mathbf{f}_\pm(r) \exp[i(k_{z\pm}z - \omega_0 t + l\varphi)], \tag{B1}$$

where l represents the topological charge. In the cylindrical coordinate system,

$$\nabla \times \mathbf{F}_\pm = \pm k_\pm \mathbf{F}_\pm, \quad \nabla^2\mathbf{F}_\pm + k_\pm^2 \mathbf{F}_\pm = 0 \tag{B2}$$

can be written as

$$\nabla^2 F_{\pm r} - \frac{2}{r^2}\frac{\partial F_{\pm\varphi}}{\partial\varphi} - \frac{F_{\pm r}}{r^2} + k_\pm^2 F_{\pm r} = 0, \tag{B3a}$$

$$\nabla^2 F_{\pm\varphi} + \frac{2}{r^2}\frac{\partial F_{\pm r}}{\partial\varphi} - \frac{F_{\pm\varphi}}{r^2} + k_\pm^2 F_{\pm\varphi} = 0, \tag{B3b}$$

$$\nabla^2 F_{\pm z} + k_\pm^2 F_{\pm z} = 0. \tag{B3c}$$

Substituting Eq. (B1) into Eq. (B3c), we can obtain

$$\frac{1}{r}\frac{\partial}{\partial r}\left(r\frac{\partial f_{\pm z}}{\partial r}\right) + \left(k_\pm^2 - k_{z\pm}^2 - \frac{l^2}{r^2}\right)f_{\pm z} = 0, \tag{B4}$$

which is a Bessel function with general solution

$$f_{\pm z} = a_\pm J_l(k_r r)e^{il\varphi}e^{-i\omega_0 t}e^{ik_{z\pm}z}, \tag{B5}$$

where $k_r^2 = k_\pm^2 - k_{z\pm}^2$, $a_\pm$ is arbitrary constant, and J_l is the lth-order Bessel function of the first kind.

Secondly, on the other hand, we construct Bessel beams in chiral medium from the superposition of plane waves with the same frequency $\omega = \omega_0$. Consider such a beam propagates along the z axis. In the paraxial approximation, all the plane waves' vectors $\mathbf{k}$ are distributed within a cone of polar angle θ_0 ($\theta_0 \ll 1$), and each wave vector carries an accompanying azimuthal phase difference $l\phi$ (note ϕ is in the k-space and l is the topological charge), as depicted in Fig. 6. In achiral medium (air), the real-space wave function can be obtained as a Fourier-type integral:

$$\psi(\mathbf{r}, t) \propto \int_0^{2\pi} e^{i[k_\parallel z + k_\perp \cos(\phi)x + k_\perp \sin(\phi)y + l\phi - \omega_0 t]}d\phi$$

$$\propto J_l(k_\perp r)\exp(ik_\parallel z + il\varphi - i\omega_0 t), \tag{B6}$$

where $k_z = k_\parallel = k_0 \cos\theta_0$, $k_\perp = k_0 \sin\theta_0$, and $k_0 = \omega_0/c$.

Conversely, we can construct the Bessel beam in chiral medium by considering the aforementioned Bessel beam transmitted normally from air to the chiral medium. Two eigenmodes (RCP and LCP) are supported in the chiral medium, and they both obey Snell's law $\sin\theta_0 = n_+ \sin\theta_+ = n_- \sin\theta_-$, where $n_\pm = n_0 \pm \xi$, n_0 is the medium refractive index, and ξ is the chirality parameter. Thus, for each plane wave in the k-space, $k_0 \sin\theta_0 = k_0 n_+ \sin\theta_+ = k_0 n_- \sin\theta_-$ and
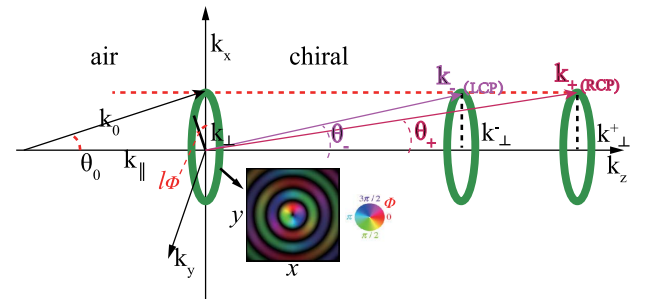

Fig. 6. Plane wave spectra in air (left) and a chiral medium (right). The colorful inset depicts the phase-intensity distributions of real-space wave functions for the monochromatic Bessel beam with $l = 1$, where the brightness is proportional to the intensity, while the color indicates the phase.

$k_0 \sin \theta_0 = k_+ \sin \theta_+ = k_- \sin \theta_-$. We then know that $k_\perp = k_\perp^+ = k_\perp^-$ for each plane wave with preserved azimuthal phase difference $l\phi$. Therefore, the real-space wave function can be obtained as a Fourier-type integral:

$$\psi(\mathbf{r}, t) = a_+ \int_0^{2\pi} e^{i[k_\parallel^+ z + k_\perp \cos(\phi)x + k_\perp \sin(\phi)y + l\phi - \omega_0 t]} d\phi$$
$$+ a_- \int_0^{2\pi} e^{i[k_\parallel^- z + k_\perp \cos(\phi)x + k_\perp \sin(\phi)y + l\phi - \omega_0 t]} d\phi$$
$$= [a_+ J_l(k_\perp r) \exp(ik_\parallel^+ z + il\varphi - i\omega_0 t)$$
$$+ a_- J_l(k_\perp r) \exp(ik_\parallel^- z + il\varphi - i\omega_0 t)], \quad \text{(B7)}$$

where $a_\pm$ represents the amplitude constants, and $k_\parallel^+ = k_+$ and $k_\parallel^- = k_-$ in the paraxial approximation.

As a result, deduction based on Maxwell's equations and construction from the Fourier integral of superposition of plane waves in the k-space lead to the same Bessel beam solution in the chiral medium. This confirms the correctness of both approaches. The problem-solving logic in the second approach tells us that the RCP and LCP eigenmodes should share the same rotational and translational symmetry simultaneously. This paves the way of our next deductions of spin skyrmion/meron lattices.

APPENDIX C: METAL-CHIRAL-METAL SPIN SKYRMION LATTICE OF BLOCH-TYPE

Let us first start from a simpler case, i.e., vortex SPPs at a chiral-metal single interface. For an evanescent wave decaying exponentially along the z direction on the surface of a chiral medium, $F_{\pm z}$ can be expressed as $F_{\pm z} = \Psi_\pm e^{-k_{\pm z} z}$; thus,

$$\nabla^2 F_{\pm z} + k_\pm^2 F_{\pm z} = 0 \quad \text{(C1)}$$

can be written as

$$\frac{\partial^2 \Psi_{XY}^\pm}{\partial x^2} + \frac{\partial^2 \Psi_{XY}^\pm}{\partial y^2} + k_r^2 \Psi_{XY}^\pm = 0, \quad \text{(C2)}$$

where $k_r^2 = k_\pm^2 + k_{\pm z}^2$. Assuming a hexagonal periodicity of the EM field, $\Psi_{XY}^\pm$ should fulfill a translational symmetry as expressed by

$$\Psi_{XY}^\pm(x + L_x, y) = \Psi_{XY}^\pm(x, y),$$
$$\Psi_{XY}^\pm(x, y + L_y) = \Psi_{XY}^\pm(x, y), \quad \text{(C3)}$$

where L_x and L_y have a scaling factor of $\sqrt{3}$. On the other hand, one can find that, for the generated optical lattice, $L_x = 2\lambda_r$ and $L_y = 2/\sqrt{3}\lambda_r$, where $\lambda_r = 2\pi/k_r$. Besides the translational symmetry, the optical lattice also possesses certain degrees of rotational symmetry, which is related to the topological charge (l) of the vortex:

$$R_z(\alpha)\Psi_{XY}^\pm[R_z(-\alpha)\vec{r}] = e^{il\alpha}\Psi_{XY}^\pm(\vec{r}). \quad \text{(C4)}$$

By taking into account three special cases for α in the rotation matrix with respect to the z axis as $\alpha = -\pi/3, \pi/3$, and π, and assuming $l = 1$, one can finally obtain [$\theta_n = n\pi/N$, $\mathbf{e}_n = (\cos\theta_n, \sin\theta_n)$ with $N = 3$ for hexagonal and $N = 2$ for square lattice]

$$F_{\pm z} = a_\pm e^{-k_{\pm z} z} \sum_{n=1}^{2N} e^{il\theta_n} e^{ik_r \mathbf{r} \cdot \mathbf{e}_n} = a_\pm e^{-k_{\pm z} z}$$
$$\times \left[\left(\frac{1}{\sqrt{3}} + i\right) \sin\left(\frac{1}{2}k_r x + \frac{\sqrt{3}}{2}k_r y\right) + \left(\frac{1}{\sqrt{3}} - i\right) \sin\left(\frac{1}{2}k_r x - \frac{\sqrt{3}}{2}k_r y\right) + \frac{2}{\sqrt{3}} \sin(k_r x) \right]$$
$$= a_\pm e^{-k_{\pm z} z} \frac{2}{\sqrt{3}} \left[e^{i\frac{\pi}{3}} \sin\left(\frac{1}{2}k_r x + \frac{\sqrt{3}}{2}k_r y\right) + e^{-i\frac{\pi}{3}} \sin\left(\frac{1}{2}k_r x - \frac{\sqrt{3}}{2}k_r y\right) + \sin(k_r x) \right],$$

$$F_{+x} = a_{1+} e^{-k_{z+}(z+d)} \frac{1}{k_r} \left\{ k_+ \left[e^{i\frac{\pi}{3}} \cos\left(\frac{1}{2}k_r x + \frac{\sqrt{3}}{2}k_r y\right) - e^{-i\frac{\pi}{3}} \cos\left(\frac{1}{2}k_r x - \frac{\sqrt{3}}{2}k_r y\right) \right] \right.$$
$$\left. - \frac{1}{\sqrt{3}} k_{z+} \left[e^{i\frac{\pi}{3}} \cos\left(\frac{1}{2}k_r x + \frac{\sqrt{3}}{2}k_r y\right) + e^{-i\frac{\pi}{3}} \cos\left(\frac{1}{2}k_r x - \frac{\sqrt{3}}{2}k_r y\right) + 2 \cos(k_r x) \right] \right\}$$
$$+ a_{2+} e^{k_{z+}(z-d)} \frac{1}{k_r} \left\{ k_+ \left[e^{i\frac{\pi}{3}} \cos\left(\frac{1}{2}k_r x + \frac{\sqrt{3}}{2}k_r y\right) - e^{-i\frac{\pi}{3}} \cos\left(\frac{1}{2}k_r x - \frac{\sqrt{3}}{2}k_r y\right) \right] \right.$$
$$\left. + \frac{1}{\sqrt{3}} k_{z+} \left[e^{i\frac{\pi}{3}} \cos\left(\frac{1}{2}k_r x + \frac{\sqrt{3}}{2}k_r y\right) + e^{-i\frac{\pi}{3}} \cos\left(\frac{1}{2}k_r x - \frac{\sqrt{3}}{2}k_r y\right) + 2 \cos(k_r x) \right] \right\},$$

$$F_{-x} = a_{1-}e^{-k_{z-}(z+d)}\frac{1}{k_r}\left\{-k_-\left[e^{i\frac{\pi}{3}}\cos\left(\frac{1}{2}k_rx+\frac{\sqrt{3}}{2}k_ry\right)-e^{-i\frac{\pi}{3}}\cos\left(\frac{1}{2}k_rx-\frac{\sqrt{3}}{2}k_ry\right)\right]\right.$$

$$-\frac{1}{\sqrt{3}}k_{z-}\left[e^{i\frac{\pi}{3}}\cos\left(\frac{1}{2}k_rx+\frac{\sqrt{3}}{2}k_ry\right)+e^{-i\frac{\pi}{3}}\cos\left(\frac{1}{2}k_rx-\frac{\sqrt{3}}{2}k_ry\right)+2\cos(k_rx)\right]\right\}$$

$$+a_{2-}e^{k_{z-}(z-d)}\frac{1}{k_r}\left\{-k_-\left[e^{i\frac{\pi}{3}}\cos\left(\frac{1}{2}k_rx+\frac{\sqrt{3}}{2}k_ry\right)-e^{-i\frac{\pi}{3}}\cos\left(\frac{1}{2}k_rx-\frac{\sqrt{3}}{2}k_ry\right)\right]\right.$$

$$\left.+\frac{1}{\sqrt{3}}k_{z-}\left[e^{i\frac{\pi}{3}}\cos\left(\frac{1}{2}k_rx+\frac{\sqrt{3}}{2}k_ry\right)+e^{-i\frac{\pi}{3}}\cos\left(\frac{1}{2}k_rx-\frac{\sqrt{3}}{2}k_ry\right)+2\cos(k_rx)\right]\right\},$$

$$F_{+y} = a_{1+}e^{-k_{z+}(z+d)}\frac{1}{k_r}\left\{-k_{z+}\left[e^{i\frac{\pi}{3}}\cos\left(\frac{1}{2}k_rx+\frac{\sqrt{3}}{2}k_ry\right)-e^{-i\frac{\pi}{3}}\cos\left(\frac{1}{2}k_rx-\frac{\sqrt{3}}{2}k_ry\right)\right]\right.$$

$$\left.-\frac{1}{\sqrt{3}}k_+\left[e^{i\frac{\pi}{3}}\cos\left(\frac{1}{2}k_rx+\frac{\sqrt{3}}{2}k_ry\right)+e^{-i\frac{\pi}{3}}\cos\left(\frac{1}{2}k_rx-\frac{\sqrt{3}}{2}k_ry\right)+2\cos(k_rx)\right]\right\}$$

$$+a_{2+}e^{k_{z+}(z-d)}\frac{1}{k_r}\left\{k_{z+}\left[e^{i\frac{\pi}{3}}\cos\left(\frac{1}{2}k_rx+\frac{\sqrt{3}}{2}k_ry\right)-e^{-i\frac{\pi}{3}}\cos\left(\frac{1}{2}k_rx-\frac{\sqrt{3}}{2}k_ry\right)\right]\right.$$

$$\left.-\frac{1}{\sqrt{3}}k_+\left[e^{i\frac{\pi}{3}}\cos\left(\frac{1}{2}k_rx+\frac{\sqrt{3}}{2}k_ry\right)+e^{-i\frac{\pi}{3}}\cos\left(\frac{1}{2}k_rx-\frac{\sqrt{3}}{2}k_ry\right)+2\cos(k_rx)\right]\right\},$$

$$F_{-y} = a_{1-}e^{-k_{z-}(z+d)}\frac{1}{k_r}\left\{-k_{z-}\left[e^{i\frac{\pi}{3}}\cos\left(\frac{1}{2}k_rx+\frac{\sqrt{3}}{2}k_ry\right)-e^{-i\frac{\pi}{3}}\cos\left(\frac{1}{2}k_rx-\frac{\sqrt{3}}{2}k_ry\right)\right]\right.$$

$$\left.+\frac{1}{\sqrt{3}}k_-\left[e^{i\frac{\pi}{3}}\cos\left(\frac{1}{2}k_rx+\frac{\sqrt{3}}{2}k_ry\right)+e^{-i\frac{\pi}{3}}\cos\left(\frac{1}{2}k_rx-\frac{\sqrt{3}}{2}k_ry\right)+2\cos(k_rx)\right]\right\}$$

$$+a_{2-}e^{k_{z-}(z-d)}\frac{1}{k_r}\left\{k_{z-}\left[e^{i\frac{\pi}{3}}\cos\left(\frac{1}{2}k_rx+\frac{\sqrt{3}}{2}k_ry\right)-e^{-i\frac{\pi}{3}}\cos\left(\frac{1}{2}k_rx-\frac{\sqrt{3}}{2}k_ry\right)\right]\right.$$

$$\left.+\frac{1}{\sqrt{3}}k_-\left[e^{i\frac{\pi}{3}}\cos\left(\frac{1}{2}k_rx+\frac{\sqrt{3}}{2}k_ry\right)+e^{-i\frac{\pi}{3}}\cos\left(\frac{1}{2}k_rx-\frac{\sqrt{3}}{2}k_ry\right)+2\cos(k_rx)\right]\right\},\tag{C5}$$

$$S_x = \frac{\varepsilon}{8\omega k_r}\times\left\{[a_{1+}^2 k_{z+}e^{-2k_{z+}(z+d)}+a_{1-}^2 k_{z-}e^{-2k_{z-}(z+d)}-a_{2+}^2 k_{z+}e^{2k_{z+}(z-d)}-a_{2-}^2 k_{z-}e^{2k_{z-}(z-d)}]S_{x0}\right.$$

$$\left.-\frac{1}{\sqrt{3}}\{[a_{1+}e^{-k_{z+}(z+d)}+a_{2+}e^{k_{z+}(z-d)}]^2 k_+ - [a_{1-}^2 k_- e^{-k_{z-}(z+d)}+a_{2-}e^{k_{z-}(z-d)}]^2 k_-\}S_{y0}\right\},$$

$$S_y = \frac{\varepsilon}{8\omega k_r}\times\left\{\{[a_{1+}e^{-k_{z+}(z+d)}+a_{2+}e^{k_{z+}(z-d)}]^2 k_+ - [a_{1-}^2 k_- e^{-k_{z-}(z+d)}+a_{2-}e^{k_{z-}(z-d)}]^2 k_-\}S_{x0}\right.$$

$$\left.+\frac{1}{\sqrt{3}}[a_{1+}^2 k_{z+}e^{-2k_{z+}(z+d)}+a_{1-}^2 k_{z-}e^{-2k_{z-}(z+d)}-a_{2+}^2 k_{z+}e^{2k_{z+}(z-d)}-a_{2-}^2 k_{z-}e^{2k_{z-}(z-d)}]S_{y0}\right\},\tag{C6}$$

$$S_{x0} = 2\sin(k_rx)+\sin\left(\frac{1}{2}k_rx+\frac{\sqrt{3}}{2}k_ry\right)+\sin\left(\frac{1}{2}k_rx-\frac{\sqrt{3}}{2}k_ry\right)+\sin\left(\frac{3}{2}k_rx+\frac{\sqrt{3}}{2}k_ry\right)+\sin\left(\frac{3}{2}k_rx-\frac{\sqrt{3}}{2}k_ry\right),$$

$$S_{y0} = 2\sin(\sqrt{3}k_ry)+\sin\left(\frac{3}{2}k_rx+\frac{\sqrt{3}}{2}k_ry\right)-\sin\left(\frac{3}{2}k_rx-\frac{\sqrt{3}}{2}k_ry\right)+3\sin\left(\frac{1}{2}k_rx+\frac{\sqrt{3}}{2}k_ry\right)-3\sin\left(\frac{1}{2}k_rx-\frac{\sqrt{3}}{2}k_ry\right).\tag{C7}$$

APPENDIX D: METAL-CHIRAL-METAL SPIN MERON LATTICE OF BLOCH TYPE

Setting $N = 2$, we get the field expressions for an MCM spin lattice:

$$F_{+x} = -\frac{1}{k_r}\{a_{1+}e^{-k_{z+}(z+d)}[ik_{z+}\cos(k_rx) + k_+\cos(k_ry)] \\ + a_{2+}e^{k_{z+}(z-d)}[-ik_{z+}\cos(k_rx) + k_+\cos(k_ry)]\},$$

$$F_{-x} = -\frac{1}{k_r}\{a_{1-}e^{-k_{z-}(z+d)}[ik_{z-}\cos(k_rx) - k_-\cos(k_ry)] \\ + a_{2-}e^{k_{z-}(z-d)}[-ik_{z-}\cos(k_rx) - k_-\cos(k_ry)]\},$$

$$F_{+y} = -\frac{1}{k_r}\{a_{1+}e^{-k_{z+}(z+d)}[ik_+\cos(k_rx) - k_{z+}\cos(k_ry)] \\ + a_{2+}e^{k_{z+}(z-d)}[ik_+\cos(k_rx) + k_{z+}\cos(k_ry)]\},$$

$$F_{-y} = -\frac{1}{k_r}\{a_{1-}e^{-k_{z-}(z+d)}[-ik_-\cos(k_rx) - k_{z-}\cos(k_ry)] \\ + a_{2-}e^{k_{z-}(z-d)}[-ik_-\cos(k_rx) + k_{z-}\cos(k_ry)]\},$$

$$F_{+z} = [a_{1+}e^{-k_{z+}(z+d)} + a_{2+}e^{k_{z+}(z-d)}] \times [i\sin(k_rx) - \sin(k_ry)],$$
$$F_{-z} = [a_{1-}e^{-k_{z-}(z+d)} + a_{2-}e^{k_{z-}(z-d)}] \times [i\sin(k_rx) - \sin(k_ry)].$$

(D1)

Therefore, the SAM for the MCM spin meron lattice can be written as

$$S_{x,y} = \frac{\varepsilon}{8\omega k_r}\{\{\sin(k_rx + k_ry) \times [a_{1+}^2 k_{z+}e^{-2k_{z+}(z+d)} \\ + a_{1-}^2 k_{z-}e^{-2k_{z-}(z+d)} - a_{2+}^2 k_{z+}e^{2k_{z+}(z-d)} - a_{2-}^2 k_{z-}e^{2k_{z-}(z-d)}] \\ \mp \{[a_{1+}e^{-k_{z+}(z+d)} + a_{2+}e^{k_{z+}(z-d)}]^2 k_+ \\ - [a_{1-}^2 k_- e^{-k_{z-}(z+d)} + a_{2-}e^{k_{z-}(z-d)}]^2 k_-\}\} + \sin(k_rx - k_ry) \\ \times \{\pm[a_{1+}^2 k_{z+}e^{-2k_{z+}(z+d)} + a_{1-}^2 k_{z-}e^{-2k_{z-}(z+d)} \\ - a_{2+}^2 k_{z+}e^{2k_{z+}(z-d)} - a_{2-}^2 k_{z-}e^{2k_{z-}(z-d)}] \\ + \{[a_{1+}e^{-k_{z+}(z+d)} + a_{2+}e^{k_{z+}(z-d)}]^2 k_+ \\ - [a_{1-}^2 k_- e^{-k_{z-}(z+d)} + a_{2-}e^{k_{z-}(z-d)}]^2 k_-\}\}\},$$

(D2)

where the super- and subscripts in the signs $\mp$ or $\pm$ of equation correspond to S_x and S_y, respectively.

REFERENCES

1. X. Yin and C. Peng, "Manipulating light radiation from a topological perspective," Photon. Res. **8**, B25–B38 (2020).
2. J. Chen, C. Wan, and Q. Zhan, "Engineering photonic angular momentum with structured light: a review," Adv. Photon. **3**, 064001 (2021).
3. X. Z. Yu, W. Koshibae, Y. Tokunaga, K. Shibata, Y. Taguchi, N. Nagaosa, and Y. Tokura, "Transformation between meron and skyrmion topological spin textures in a chiral magnet," Nature **564**, 95–98 (2018).
4. T. Skyrme, "A unified field theory of mesons and baryons," Nucl. Phys. **31**, 556–569 (1962).
5. S. Tsesses, E. Ostrovsky, K. Cohen, B. Gjonaj, N. H. Lindner, and G. Bartal, "Optical skyrmion lattice in evanescent electromagnetic fields," Science **361**, 993–996 (2018).
6. L. Du, A. Yang, A. V. Zayats, and X. Yuan, "Deep-subwavelength features of photonic skyrmions in a confined electromagnetic field with orbital angular momentum," Nat. Phys. **15**, 650–654 (2019).
7. N. Rivera and I. Kaminer, "Light–matter interactions with photonic quasiparticles," Nat. Rev. Phys. **2**, 538–561 (2020).
8. Z. Chen and M. Segev, "Highlighting photonics: looking into the next decade," eLight **1**, 2 (2021).
9. T. J. Davis, D. Janoschka, P. Dreher, B. Frank, F.-J. Meyer zu Heringdorf, and H. Giessen, "Ultrafast vector imaging of plasmonic skyrmion dynamics with deep subwavelength resolution," Science **368**, eaba6415 (2020).
10. Y. Dai, Z. Zhou, A. Ghosh, R. S. K. Mong, A. Kubo, C.-B. Huang, and H. Petek, "Plasmonic topological quasiparticle on the nanometre and femtosecond scales," Nature **588**, 616–619 (2020).
11. S. Tsesses, K. Cohen, E. Ostrovsky, B. Gjonaj, and G. Bartal, "Spin–orbit interaction of light in plasmonic lattices," Nano Lett. **19**, 4010–4016 (2019).
12. C. C. Li, P. Shi, L. P. Du, and X. C. Yuan, "Mapping the near-field spin angular momenta in the structured surface plasmon polariton field," Nanoscale **12**, 13674–13679 (2020).
13. C. Bai, J. Chen, Y. Zhang, D. Zhang, and Q. Zhan, "Dynamic tailoring of an optical skyrmion lattice in surface plasmon polaritons," Opt. Express **28**, 10320–10328 (2020).
14. Z.-L. Deng, T. Shi, A. Krasnok, X. Li, and A. Alù, "Observation of topologically robust localized magnetic plasmon skyrmions," Nat. Commun. **13**, 8 (2021).
15. M. Lin, W. Zhang, C. Liu, L. Du, and X. Yuan, "Photonic spin skyrmion with dynamic position control," ACS Photon. **8**, 2567–2572 (2021).
16. T. V. Mechelen and Z. Jacob, "Photonic Dirac monopoles and skyrmions: spin-1 quantization [invited]," Opt. Mater. Express **9**, 95–111 (2019).
17. S. Gao, F. C. Speirits, F. Castellucci, S. Franke-Arnold, S. M. Barnett, and J. B. Götte, "Paraxial skyrmionic beams," Phys. Rev. A **102**, 053513 (2020).
18. R. Gutiérrez-Cuevas and E. Pisanty, "Optical polarization skyrmionic fields in free space," J. Opt. **23**, 024004 (2021).
19. J. Zhu, S. Liu, and Y.-S. Zhang, "Synthesis and observation of optical skyrmionic structure in free space," arXiv:2103.11293 (2021).
20. Y. Shen, E. C. Martínez, and C. Rosales-Guzmán, "Generation of tunable optical skyrmions on Skyrme-Poincaré sphere," arXiv:2107.04394 (2021).

21. W. Lin, Y. Ota, Y. Arakawa, and S. Iwamoto, "Microcavity-based generation of full Poincaré beams with arbitrary skyrmion numbers," Phys. Rev. Res. **3**, 023055 (2021).

22. A. Karnieli, S. Tsesses, G. Bartal, and A. Arie, "Emulating spin transport with nonlinear optics, from high-order skyrmions to the topological Hall effect," Nat. Commun. **12**, 1092 (2021).

23. Y. Ilin, S. Tsesses, G. Bartal, and Y. Sagi, "Sub-wavelength spin excitations in ultracold gases created by stimulated Raman transitions," New J. Phys. **22**, 093071 (2020).

24. Y. Shen, Y. Hou, N. Papasimakis, and N. I. Zheludev, "Supertoroidal light pulses: propagating electromagnetic skyrmions in free space," Nat. Commun. **12**, 5891 (2021).

25. C. Guo, M. Xiao, Y. Guo, L. Yuan, and S. Fan, "Meron spin textures in momentum space," Phys. Rev. Lett. **124**, 106103 (2020).

26. M. Król, H. Sigurdsson, K. Rechcińska, P. Oliwa, K. Tyszka, W. Bardyszewski, A. Opala, M. Matuszewski, P. Morawiak, R. Mazur, W. Piecek, P. Kula, P. G. Lagoudakis, B. Piętka, and J. Szczytko, "Observation of second-order meron polarization textures in optical microcavities," Optica **8**, 255–261 (2021).

27. X. Lei, A. Yang, P. Shi, Z. Xie, L. Du, A. V. Zayats, and X. Yuan, "Photonic spin lattices: symmetry constraints for skyrmion and meron topologies," Phys. Rev. Lett. **127**, 237403 (2021).

28. Y. Shen, "Topological bimeronic beams," Opt. Lett. **46**, 3737–3740 (2021).

29. S. B. Wang and C. T. Chan, "Lateral optical force on chiral particles near a surface," Nat. Commun. **5**, 3307 (2014).

30. K. Y. Bliokh, D. Smirnova, and F. Nori, "Quantum spin Hall effect of light," Science **348**, 1448–1451 (2015).

31. T. V. Mechelen and Z. Jacob, "Universal spin-momentum locking of evanescent waves," Optica **3**, 118–126 (2016).

32. P. Shi, L. Du, C. Li, A. Zayats, and X. Yuan, "Transverse spin dynamics in structured electromagnetic guided waves," Proc. Natl. Acad. Sci. USA **118**, e2018816118 (2021).

33. A. Fert, N. Reyren, and V. Cros, "Magnetic skyrmions: advances in physics and potential applications," Nat. Rev. Mater. **2**, 17031 (2017).

34. A. N. Bogdanov and C. Panagopoulos, "Physical foundations and basic properties of magnetic skyrmions," Nat. Rev. Phys. **2**, 492–498 (2020).

35. S.-H. Yang, "Spintronics on chiral objects," Appl. Phys. Lett. **116**, 120502 (2020).

36. L. Du, A. Yang, and X. Yuan, "Ultrasensitive displacement sensing method and device based on local spin characteristics," U.S. Patent Application, 20210223165 (2021).

37. Q. Zhang, Z. Liu, F. Qin, S. J. Zeng, D. Zhang, Z. Gu, X. Liu, and J.-J. Xiao, "Exploring optical resonances of nanoparticles excited by optical skyrmion lattices," Opt. Express **27**, 7009–7022 (2019).

38. J. Wätzel and J. Berakdar, "Topological light fields for highly nonlinear charge quantum dynamics and high harmonic generation," Opt. Express **28**, 19469–19481 (2020).

39. X.-G. Wang, L. Chotorlishvili, N. Arnold, V. K. Dugaev, I. Maznichenko, J. Barnaś, P. A. Buczek, S. S. P. Parkin, and A. Ernst, "Plasmonic skyrmion lattice based on the magnetoelectric effect," Phys. Rev. Lett. **125**, 227201 (2020).

40. X. Lei, L. Du, X. Yuan, and A. V. Zayats, "Optical spin–orbit coupling in the presence of magnetization: photonic skyrmion interaction with magnetic domains," Nanophotonics **10**, 3667–3675 (2021).

41. T. Meiler, B. Frank, and H. Giessen, "Dynamic tailoring of an optical skyrmion lattice in surface plasmon polaritons: comment," Opt. Express **28**, 33614–33615 (2020).

42. C. Bai, J. Chen, D. Zhang, and Q. Zhan, "Dynamic tailoring of an optical skyrmion lattice in surface plasmon polaritons: reply," Opt. Express **28**, 33616–33618 (2020).

43. G. Mi and V. Van, "Characteristics of surface plasmon polaritons at a chiral–metal interface," Opt. Lett. **39**, 2028–2031 (2014).

44. H. Ge, X.-Y. Xu, L. Liu, R. Xu, Z.-K. Lin, S.-Y. Yu, M. Bao, J.-H. Jiang, M.-H. Lu, and Y.-F. Chen, "Observation of acoustic skyrmions," Phys. Rev. Lett. **127**, 144502 (2021).

45. S. Quabis, R. Dorn, and G. Leuchs, "Generation of a radially polarized doughnut mode of high quality," Appl. Phys. B **81**, 597–600 (2005).

46. C.-F. Kuo and S.-C. Chu, "Dynamic control of the interference pattern of surface plasmon polaritons and its application to particle manipulation," Opt. Express **26**, 19123–19136 (2018).

47. F. Träger, *Springer Handbook of Lasers and Optics* (Springer, 2012).

48. I. V. Lindell, A. H. Sihvola, S. A. Tretyakov, and A. J. Viitanen, *Electromagnetic Waves in Chiral and Bi-Isotropic Media* (Artech House, 1994).

49. C. Kelly, L. Khosravi Khorashad, N. Gadegaard, L. D. Barron, A. O. Govorov, A. S. Karimullah, and M. Kadodwala, "Controlling metamaterial transparency with superchiral fields," ACS Photon. **5**, 535–543 (2018).

50. C. F. Bohren, "Light scattering by an optically active sphere," Chem. Phys. Lett. **29**, 458–462 (1974).

51. N. Nagaosa and Y. Tokura, "Topological properties and dynamics of magnetic skyrmions," Nat. Nanotechnol. **8**, 899–911 (2013).

52. P. Shi, L. Du, M. Li, and X. Yuan, "Symmetry-protected photonic chiral spin textures by spin–orbit coupling," Laser Photon. Rev. **15**, 2000554 (2021).

53. Q. Zhang, Z. Xie, L. Du, P. Shi, and X. Yuan, "Bloch-type photonic skyrmions in optical chiral multilayers," Phys. Rev. Res. **3**, 023109 (2021).

54. X. Zhang, Q. Xu, L. Xia, Y. Li, J. Gu, Z. Tian, C. Ouyang, J. Han, and W. Zhang, "Terahertz surface plasmonic waves: a review," Adv. Photon. **2**, 014001 (2020).

55. J. S. T. Smalley, F. Vallini, X. Zhang, and Y. Fainman, "Dynamically tunable and active hyperbolic metamaterials," Adv. Opt. Photon. **10**, 354–408 (2018).

56. G. Hu, Q. Ou, G. Si, Y. Wu, J. Wu, Z. Dai, A. Krasnok, Y. Mazor, Q. Zhang, Q. Bao, C.-W. Qiu, and A. Alù, "Topological polaritons and photonic magic angles in twisted α-MoO₃ bilayers," Nature **582**, 209–213 (2020).

57. X. Lin, Z. Liu, T. Stauber, G. Gómez-Santos, F. Gao, H. Chen, B. Zhang, and T. Low, "Chiral plasmons with twisted atomic bilayers," Phys. Rev. Lett. **125**, 077401 (2020).

58. G. Hu, C. Zheng, J. Ni, C.-W. Qiu, and A. Alù, "Enhanced light-matter interactions at photonic magic-angle topological transitions," Appl. Phys. Lett. **118**, 211101 (2021).

59. H. Zhao, X. Chen, C. Ouyang, H. Wang, D. Kong, P. Yang, B. Zhang, C. Wang, G. Wei, T. Nie, W. Zhao, J. Miao, Y. Li, L. Wang, and X. Wu, "Generation and manipulation of chiral terahertz waves in the three-dimensional topological insulator Bi₂Te₃," Adv. Photon. **2**, 066003 (2020).

60. M. Jung, R. Gladstone, and G. Shvets, "Nanopolaritonic second-order topological insulator based on graphene plasmons," Adv. Photon. **2**, 046003 (2020).

61. Q. Yan, Q. Chen, L. Zhang, R. Xi, H. Chen, and Y. Yang, "Unconventional Weyl exceptional contours in non-Hermitian photonic continua," Photon. Res. **9**, 2435–2442(2021).

62. H. Zhang, S. Xia, Y. Zhang, Y. Li, D. Song, C. Liu, and Z. Zhang, "Nonlinear topological valley Hall edge states arising from type-II Dirac cones," Adv. Photon. **3**, 056001 (2021).